Link between divertor conditions and HFS/LFS midplane density profiles in H-mode plasmas at ASDEX Upgrade

L. Guimarais[1], C. Silva[1], M. Bernert[2], D. Brida[2], M. Cavedon[2], G. D. Conway[2], A. Drenik[2], L. Gil[1], T. Reichbauer[2], F. Reimold[3], J. Santos[1], E. Seliunin[1], A. Silva[1], U. Stroth[2,4], J. Vicente[1], E. Wolfrum[2], the ASDEX Upgrade Team and the EUROfusion MST1 team*

[1] Instituto de Plasmas e Fusão Nuclear, Instituto Superior Técnico, Universidade de Lisboa, Portugal

[2] Max-Planck-Institut für Plasmaphysik, Boltzmannstr. 2, 85748, Garching, Germany

[3] Max-Planck-Institut für Plasmaphysik, Greifswald, Germany

[4] Physik-Department E28, Technische Universität München, James-Franck-Str. 1, 85748 Garching, Germany

* See the author list of Meyer et al, Overview of physics studies on ASDEX Upgrade, Fusion Energy Conference 2018

E-mail: guimas@ipfn.tecnico.ulisboa.pt

April 2019

Abstract.

The connection between midplane and divertor conditions is studied on ASDEX Upgrade (AUG) for H-mode scenarios. H-mode discharges with variations in fuelling, heating power and impurity seeding are analysed, enabling to disentangle their impact on the evolution of midplane density profiles. The O-mode reflectometer installed on AUG provides unique insights on the midplane density profiles thanks to the ability to measure simultaneously at the high-field-side (HFS) and the low-field-side (LFS). At the inner divertor, with the onset of detachment, a region of high density is formed (HFS high density front, HFSHD) that expands into the HFS midplane, leading to strong poloidal asymmetries in the main chamber scrape-off layer (SOL) density. A good agreement is observed between the evolution of the density profiles at the midplane and that of the divertor volume density confirming the strong influence of divertor conditions on the midplane density profiles at the HFS. Our results confirm the existence of a relationship between plasma confinement, the shift in the midplane LFS density profile and the presence of the HFSHD with respect to changes in seeding and fuelling. It is established that the separatrix density at the LFS is better correlated with the neutral pressure at the outer target while the HFS SOL density follows the neutral pressure at the inner divertor. A comprehensive characterisation of the ELM evolution at the midplane and divertor is performed demonstrating that also during the ELM cycle the divertor conditions have a strong effect on the SOL density at the midplane. The most striking result is the observation of a HFSHD at the HFS midplane just after the ELM crash associated with strong inner divertor detachment.

1. Introduction

In magnetically confined fusion devices, an improvement of the particle and energy confinement time occurs above a threshold heating power (H-mode) as a result of the formation of an edge transport barrier that is associated with the increase of electron density and temperature in the pedestal region [1]. The higher heating power necessary to sustain H-modes, associated with the narrow width of the scrape-off layer (SOL) power flux profile characteristic of this confinement regime, leads to increased power loads onto the plasma facing components (PFCs) that must be mitigated. Divertor detachment [2, 3] appears as an attractive scenario for a fusion reactor. In a detached scenario, a region of high density and low temperature is formed in front of the divertor target plates, associated with large radiative losses. Detachment in H-mode requires higher plasma densities when compared to L-mode [4, 5]. In ASDEX Upgrade (AUG), with a tungsten (W) wall, only a partially detached outer target has been achieved in non-seeded H-modes so far. Partial detachment is defined as a parallel pressure loss near the strike-point, while complete detachment is characterised by a strong parallel pressure loss along a large portion of the divertor target (e.g. [6, 7]).

When gas fuelling is applied at sufficient heating power, a poloidally localised region of high density at the high-field-side (HFS) SOL appears, at the height of the X-point, the so-called HFS high density front (HFSHD)[8, 9]. Typically, the HFSHD has a density one order of magnitude larger than that at the separatrix and is associated with the detachment of the inner divertor. The HFSHD is found in both L- and H-mode plasmas and has so far been observed on AUG [8, 9] and JET [10], revealing that the presence of a HFSHD is independent of confinement mode and machine size. The HFSHD was extensively characterised in AUG density ramp discharges by Potzel et al. [9–13] using mainly spectroscopic measurements. The HFSHD was found to be correlated with neutral fluxes in the far SOL as both increase with heating power. The magnitude of the HFSHD is reduced with impurity seeding due to the radiation of the exhausted power before it reaches the HFS SOL preventing the ionisation of particles associated with the HFSHD. It was also suggested that nitrogen seeding in machines with metallic plasma facing components acts like the intrinsic radiator in carbon machines [14], thus explaining the rare observations of the HFSHD in non-metallic wall devices [8]. The HFSHD has been recovered in recent modelling of AUG with SOLPS 5.0 [15]. Drifts were found to play a crucial role in the simulations as they determine the spatial extent as well as the radial and poloidal gradients of the HFSHD. Activating drifts in the simulations leads to additional particle fluxes from the outer to the inner divertor and to increased ionisation sources in the HFS far-SOL. Modelling has shown that the HFSHD region extends along the inner target to the inner midplane in good agreement with our observations. Modelling also shows a clear in-out asymmetry of the SOL profiles and inverted gradients at the inner midplane separatrix. It was also shown that the HFSHD may play an important role in the fuelling of the core plasma as the inverted gradients could lead to a diffusive particle flow across the separatrix [15].

The midplane electron density is an important interface parameter between core (associated with fusion performance) and divertor plasma (able to control power exhaust) [16]. The separatrix density is a critical parameter for the control of divertor detachment [17]. In addition, the structure of the pedestal density plays an important role in the pedestal stability and hence in confinement, as observed in JET [18] and AUG [19]. The divertor HFSHD was suggested to lead to an outward shift of the density profile that causes a degradation of the pedestal top pressure and global confinement [19]. Unfortunately, there are conflicting requirements in terms of density; good plasma performance requires low separatrix density while handling of significant heat exhaust at the divertor requires high densities (e.g. [16]). Previous studies indicate that divertor detachment influences the core plasma confinement but the physics mechanisms behind these effects is not clear. Observations such as the increase in the low-field-side (LFS) separatrix density with fuelling and decrease with nitrogen seeding and the role of the HFSHD in defining the LFS profiles are not fully understood.

We build on previous work at AUG aiming at understanding the dynamics of the midplane edge electron density profiles on Ohmic and L-mode plasmas and its link to divertor detachment [20]. The O-mode reflectometer installed on AUG has proven to be a reliable diagnostic capable of providing unique insights on the midplane density profiles thanks to the ability to measure simultaneously at the LFS and the HFS. Reflectometry data regularly shows the existence of strong poloidal asymmetries in the SOL density that were quantified by defining an asymmetry parameter (described in detail in [20]) as the difference between the average density measured by reflectometry at the HFS and LFS, normalised to the Greenwald limit, with the profile average performed in the common radial range of the HFS and LFS reflectometry profiles in normalized radial poloidal flux coordinates.

It was shown for the first time that the region of high density on the HFS expands to the midplane, leading to strong poloidal asymmetries in the SOL density. Using the asymmetry parameter, the influence of the divertor HFSHD on the midplane radial density profiles was quantified. The evolution of the midplane edge density profile on the HFS was observed to respond to divertor oscillations, changing significantly for different divertor detachment states. An excellent agreement was found between the evolution of the density in the inner divertor measured by divertor spectroscopy and that measured by reflectometry at a corresponding radial location in the HFS midplane.

In this contribution, the evolution of the midplane density profiles is further investigated focusing now on H-mode plasmas. Again, emphasis is placed on the formation of a HFS high density region and its dependence on the fuelling rate, input power and seeding, extending the L-mode studies published before to H-mode conditions. The link between the HFSHD, divertor conditions, midplane density profiles and plasma confinement is explored. Focus is placed both on phases in between edge localised modes (ELMs), the so-called inter-ELM phase, and on the ELM evolution itself, as the bursts of energy and particles have a strong impact on the edge density profiles.

This paper is organised as follows: section 2 presents briefly the H-mode

experiments, as well as introducing the diagnostics used in this work. In section 3, an overview of detachment evolution in H-mode is given for the inter-ELM period while in section 4 the emphasis is placed on the formation of the HFSHD and its dependence on the fuelling rate and input power. In section 5 the impact of the HFSHD on midplane density profiles and confinement is discussed. In section 6 the influence of the divertor HFSHD on the midplane density evolution and the LFS/HFS profile asymmetry along the ELM cycle is analysed. Finally, a discussion of the main results is presented in section 7.

2. Experiment and diagnostic setup

Results presented in this paper were obtained in recent ASDEX Upgrade experimental campaigns where a large number of H-mode discharges were performed with variations mainly in the deuterium fuelling rates (up to $7 \times 10^{22}\,\mathrm{e/s}$) and in the external heating power ($\mathrm{P_{in}} = 2.5-18\,\mathrm{MW}$). For radiative cooling, seeding was applied (up to $2 \times 10^{22}\,\mathrm{e/s}$) via divertor valves. Although both nitrogen and neon were used in the experiment, we focus here on nitrogen seeding due to the larger dataset available. Discharges were performed in lower-single-null configuration with forward field, such that the ion ∇B drift points towards the lower divertor, with plasma current and toroidal magnetic field having opposite directions. The locations and lines of sight (LOS) of the various diagnostics used to characterise the plasma in the main SOL and divertor regions are shown in figure 1.

The O-mode microwave LFS/HFS reflectometer installed close to the machine midplane has been used in this work as the main diagnostic for the measurement of edge electron density profiles [21]. It has the unique capability of simultaneously measuring the density profiles at the HFS and LFS of the machine, covering a density range $0.3-6.0 \times 10^{19}\,\mathrm{m^{-3}}$. In this work, the individual profiles were measured every 1 ms. The frequency sweeping time for all bands is $25\,\mu$s with a dead time of $10\,\mu$s between sweeps, which is needed to stabilise the oscillators. Four consecutive frequency sweeps (taking $140\,\mu$s in total) are used to estimate each individual profile[22] that are then repeated every 1 ms [23], with the profile data stored at the average time of the four sweeps. For the discharges analysed here, LFS profile measurements were often corrupted at densities around $3.1 \times 10^{19}\,\mathrm{m^{-3}}$ due to electronic noise and therefore the highest measured density had to be restricted to this value in such cases.

The AUG broadband reflectometer performs measurements on both HFS and LFS and thus can be used to study poloidal density asymmetries inaccessible to other diagnostics. To directly compare the HFS and LFS profiles they must be mapped to normalised poloidal flux radial coordinates using a magnetic equilibrium reconstruction. However, uncertainties in the separatrix position at the HFS and LFS resulting from the magnetic equilibrium have to be considered. After the mapping procedure, data from the different diagnostics often appear to be radially displaced with respect to each other. It is a common practice to radially shift profiles from different diagnostics for

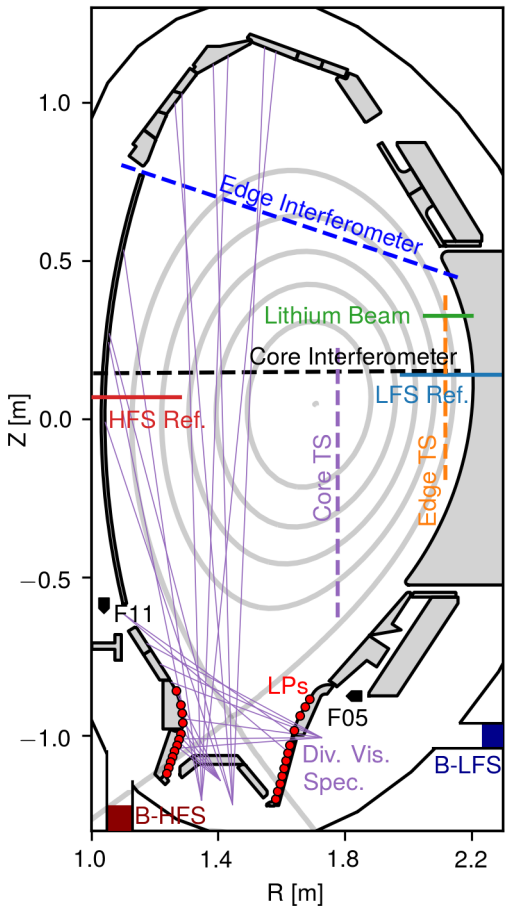

Figure 1: Diagnostic locations: Lines of sights of the LFS and HFS reflectometry (blue and red at the midplane, respectively); edge and core interferometers (dashed blue and black); divertor Langmuir probes; LOS of divertor visible spectroscopy in purple; the LFS and HFS baratrons, represented by B-HFS (dark red) and B-LFS (dark blue), respectively; the neutral pressure gauges at the inner and outer divertors, F11 and F05, respectively, with their direction represented by arrows.

density and temperature measurements in order to make the data consistent at the LFS (e.g. [24]). For the HFS, such a method is not established as, apart from reflectometry, no other diagnostic is available to provide density profiles. Therefore, the procedure to align the diagnostics was also applied to the HFS by adjusting the position of the steep gradient region so that it agrees with LFS profiles. Although the electron density is not necessarily a flux function, the steep density profiles caused by the edge transport barrier are expected to be a good reference for profile alignment between LFS and HFS diagnostics. The absence of a HFS Thomson scattering system prevents a pressure-based kinetic profile alignment for the HFS reflectometry system. The procedure to shift density profiles is illustrated in figure 2 for a discharge with a neon seeding ramp. At the HFS, steep density profiles in front of the inner wall are found when the seeding

rate is modest (figure 2a). This points to the presence of a strong density front at the inner divertor that expands up to the HFS midplane, leading to a high SOL density and to strong poloidal asymmetries in the SOL. As the seeding rate is increased the HFSHD front is mitigated, resulting in modest HFS/LFS density asymmetries in the midplane SOL. Profiles have been aligned for the case with the highest seeding rate (figure 2b) by shifting the HFS profiles by 4 cm in local diagnostic coordinates (corresponding to 2 cm at the outer midplane to which the other data are mapped) to match the steep gradient region in the confined region. The same shift is applied to the other time interval. No shift has been applied to the LFS data. The established procedure cannot be applied in discharge phases where a large HFSHD exists, as often the density at the inner wall is higher than the maximum density that can be measured. When large HFS/LFS density asymmetries are observed in the SOL, a radial shift of the LFS/HFS profiles would not make the profiles symmetric because the gradients are dramatically different.

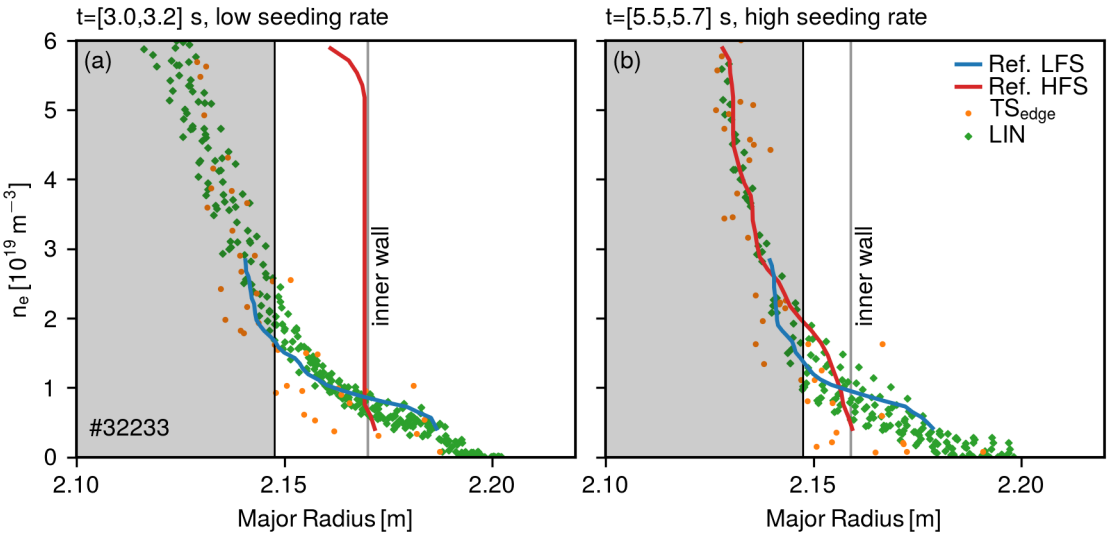

Figure 2: Example of diagnostic alignment with density measurements by reflectometry, Thomson scattering and lithium beam (LIN) diagnostics for discharge #32233 with low (left) and high (right) neon seeding rate. Reflectometry profiles have been shifted at the HFS by 2 cm while no shift has been applied to the LFS. The grey shaded area represents the confined region.

In addition to reflectometry, various other diagnostics are essential for this work with focus on divertor measurements. Divertor target Langmuir probes (LPs) [25] provide detailed information on the ion flux (Γ_{D^+}), electron density and temperature (T_e) profiles at the divertor target at the positions shown in figure 1. The neutral pressure is measured at weakly pumped ports far away from the lower divertor region by baratrons [16] and by ionisation pressure gauges [26].

The electron density in the divertor volume ($n_{e,v}$) is determined via a spectroscopic measurement of the Stark broadened D_ϵ line [13]. The spectroscopic system covers

the entire lower divertor (see figure 1, purple lines) and has a temporal resolution of 2.45 ms. By averaging measurements along the horizontal LOS indicated in figure 1, a rough indication of the inner divertor volume density is obtained. However, the field of view of the divertor spectroscopy may not cover the full spatial extension of the HFSHD. The HFSHD is sometimes located in the far-SOL above the X-point [12, 20] where the detection may have limitations.

3. Overview of the divertor detachment evolution

The effect of plasma fuelling, additional heating and seeding on pedestal conditions and plasma confinement has been explored thoroughly on AUG with the goal of optimising the design of future fusion devices (e.g. [4, 11, 16, 27, 28]).

Figure 3 presents the temporal evolution of an H-mode discharge where first the input power and the fuelling are increased and later nitrogen is injected. Three distinct discharge phases may be identified according to auxiliary heating power, fuelling and seeding levels. In the first H-mode phase, phase I, (up to 2.8 s, shaded in red), moderate NBI power and gas fuelling are applied. In phase II, (3 s to 3.5 s, shaded in green) both the NBI power and gas fuelling rate are increased. Finally, in phase III (shaded in blue) nitrogen is injected at a constant rate to cool the divertor leading to a clear enhancement in the energy confinement time. The effect of nitrogen seeding on the edge density profiles and divertor conditions may be investigated comparing phases II and III, as this is the main parameter changed between the two phases.

A practical way to visualise the large amount of profile data obtained by reflectometry is to plot the iso-density lines versus time. The temporal evolution of different density layers along the discharge can then be compared with other time-traces. Figure 3a,b shows the evolution of the LFS and HFS iso-density lines. ELMs lead to large excursions in the location of the density layers making the visualisation of the density evolution demanding. Therefore, to study the density evolution during the entire discharge it is convenient to remove the profiles measured during the ELM events when displaying iso-density lines. This is achieved by using a Kalman filter [29].

To understand the evolution of the midplane density, our attention is turned to the behaviour of the divertor parameters. The particle flux and the electron temperature measured by the target Langmuir probes near the inner and outer strike-points (figure 3e,f) are used to assess the evolution of divertor detachment. As illustrated, Γ_{D^+} increases at the inner (figure 3f) and even more noticeably at the outer target (figure 3e) when the input power is stepped up, suggesting a reduced detachment. When nitrogen is seeded, both Γ_{D^+} and T_e decrease, particularly in the inner divertor (with T_e values below 5 eV) indicating that detachment is approached. The average density in the divertor volume measured by Stark broadening, $n_{e,v}$, in the inner divertor is also shown in figure 3g. During phase II of the discharge, the density in the divertor volume increases significantly (figure 3g) indicating the development of the divertor HFSHD front, but then when nitrogen seeding is injected at a constant rate to cool the divertor,

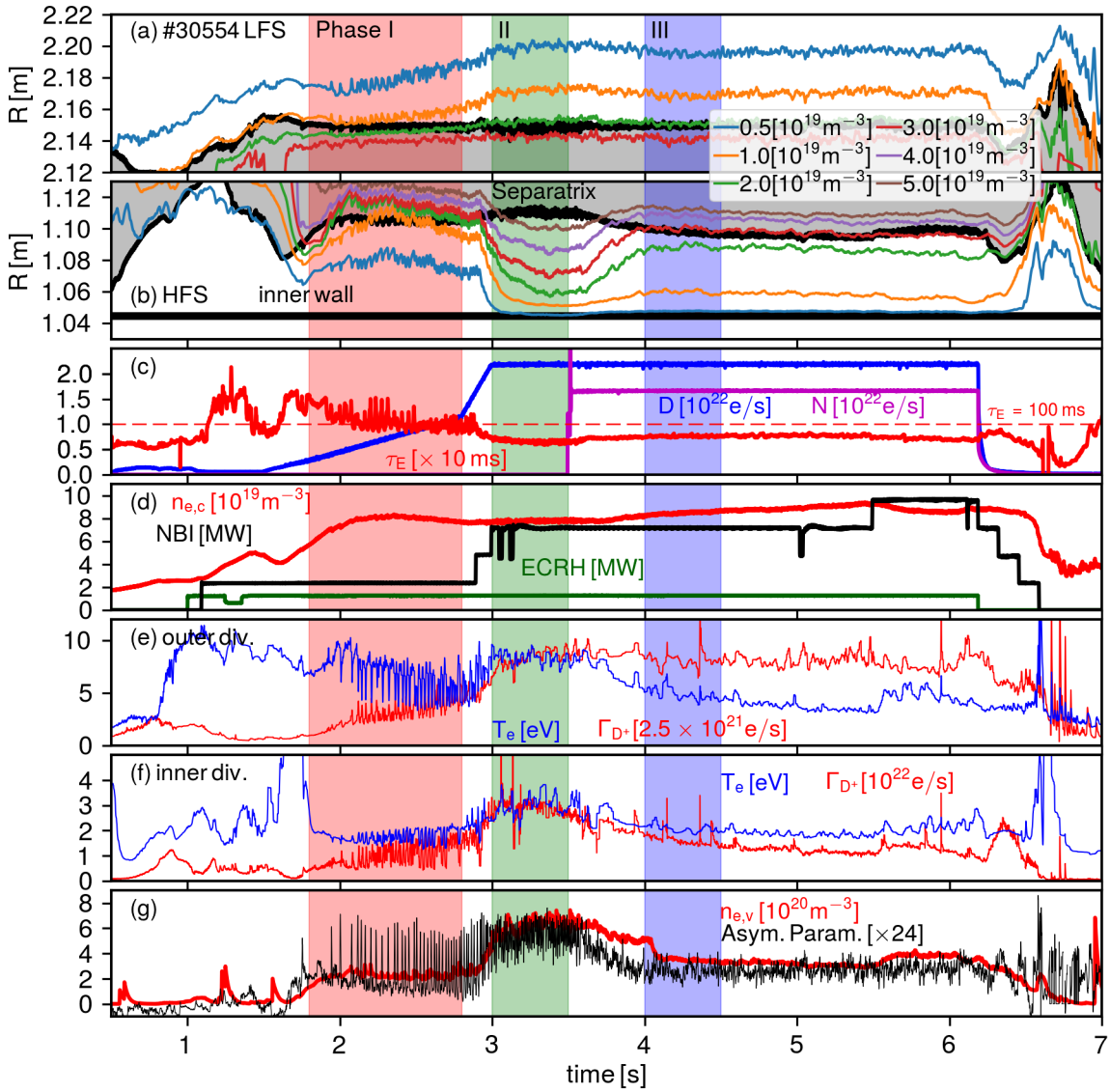

Figure 3: Iso-density layer evolution at LFS (a) and HFS (b) for discharge #30554 with nitrogen seeding from profile reflectometry; fuelling rate, nitrogen seeding rate and τ_E (c); central line-averaged density, NBI and ECRH heating power (d); Γ_{D^+} and T_e measured by Langmuir probes near the outer (e) and inner divertor strike-point (f); asymmetry parameter and density in the divertor volume (g). Reflectometry and Langmuir probe signals during ELMs have been removed. The HFS separatrix has been shifted outwards by 2 cm so that the position of the steep gradient region agrees with LFS profiles in periods where no significant poloidal asymmetries are expected (modest HFSHD) following the procedure described in section 2. The grey shaded regions in (a) and (b) represent the confined region.

the divertor HFSHD is clearly mitigated.

In spite of the roughly constant line-averaged density throughout the discharge, the behaviour of the inter-ELM midplane density profiles changes strongly. As illustrated

in figure 3a,b, in the first discharge phase the edge density profiles measured by reflectometry are roughly poloidally symmetric as expected due to the moderate values of input power and fuelling. In phase II, both the fuelling and the input power are raised leading to a stronger HFSHD at the midplane clearly identified by the quick movement of the density layers towards the inner wall (figure 3b). The density SOL width at the LFS reaches a maximum during this period as a consequence of the high fuelling rate (see figure 3a). Most of the changes at the LFS are seen in the SOL (for densities below $2 \times 10^{19}\,\mathrm{m}^{-3}$) with modest modifications in the steep gradient region. At the HFS, the HFSHD causes the density profile to approach the inner wall. The nitrogen seeding impacts on the LFS and HFS density profiles in a visibly different way. At the LFS, the SOL density is slightly reduced, seen mainly in the trajectory of the $0.5 \times 10^{19}\,\mathrm{m}^{-3}$ density layer in figure 3a, while on the HFS the effect on the average inter-ELM density profile is significantly larger: nitrogen seeding strongly moves the density layers above $0.5 \times 10^{19}\,\mathrm{m}^{-3}$ away from the inner wall as a consequence of a mitigation of the HFSHD.

Good agreement is found between the evolution of the asymmetry parameter estimated at the midplane and that of the density in the divertor measured by spectroscopy (see figure 3g), confirming the strong influence of the divertor conditions on the midplane density profiles at the HFS also in H-mode. Similarly to the observation in L-mode [20], the region of high density on the HFS expands to the midplane, leading to strong poloidal asymmetries in the SOL density. Density profiles during ELMs were not removed when calculating the asymmetry parameter, leading to strong variations during the large type-I ELMs characteristic of the first discharge phase.

A high density region is observed to develop at the inner divertor during the first phase, that then increases strongly in magnitude when the input power and fuelling are stepped-up during the second phase reaching densities in the order of $60 \times 10^{19}\,\mathrm{m}^{-3}$, in good agreement with the evolution of reflectometry data at the midplane (see figure 3g). When nitrogen is injected in the third phase the density in the divertor volume decreases, again in agreement with observations at the midplane where the LFS/HFS asymmetry in density is reduced. In this case, nitrogen actively mitigates the HFSHD without completely suppressing it as the seeding rate cannot be increased further. The HFSHD seems to be an integral part of high-power H-mode operation in AUG.

4. The role of fuelling rate and input power

With the goal of disentangling the role of fuelling rate and input power on the midplane density profiles and divertor conditions, a discharge with steps in these quantities is analysed. Three fuelling and three power steps take place independently in discharge #30733, as shown in figure 4. In order to produce a visible effect on the midplane density profiles, changes in the fuelling rate must be larger than $10^{22}\,\mathrm{e/s}$. Several time instants were chosen, indicated by the vertical coloured lines, representing the different power and/or fuelling levels. Radial profiles in normalised flux coordinates for the time instants indicated are presented in figure 5, corresponding to the vertical coloured lines of figure

4. Density profiles were averaged over 200 ms using only inter-ELM profiles. The ELM frequency is the range 110 - 180 Hz with about 50-90 profiles used for each period. The line-averaged density exhibits only a modest increase in spite of the large variation in the fuelling, as often is the case in ELMy H-mode discharges. As illustrated, Γ_{D^+} at the outer target increases with fuelling showing that this divertor region is still attached. T_e does not show significant changes throughout the discharge except a reduction at the inner target when the input power is stepped-up probably associated with an increase in the HFSHD magnitude.

As the effect of the fuelling rate and input power is different at the LFS and HFS, the two regions are analysed separately. At the LFS, the edge density is observed to respond clearly to the increase in the fuelling rate leading to an outward shift of the profile, mainly seen in the density layers below $3.0 \times 10^{19}\,\mathrm{m}^{-3}$ (see figures 4 and 5, comparing for instance profiles at t = 4.8 s and 5.5 *s*). On the contrary, the input power has a minor impact on the density profiles in the LFS SOL (comparing for instance profiles at t = 3.8 s and 4.8 s).

At the HFS, an HFSHD front exists from early on in the discharge (t > 1.5 s) as a consequence of the relatively high input power and high line-averaged density. As shown in figure 4b, the HFSHD is formed during the red-shaded interval and gets stronger when the fuelling is raised at t = 2.5 s. It increases even further when the input power is stepped up. As the density layers are already saturated (high densities measured at inner vessel wall), no further evolution is detected. A good agreement is again observed between the evolution of the density profiles at the midplane and the density in the divertor measured by spectroscopy (see figure 4c). The effect of the input power is therefore clearly different at LFS and HFS: it strongly increases the HFSHD front while the LFS profiles are not significantly modified.

Plasma confinement is also influenced by the variation in input power and fuelling (see figure 4c). Confinement is observed to degrade when either the fuelling rate or the heating power are increased, corresponding to a similar dependence on the plasma parameters than that observed for the HFSHD, which also increases with both input power and fuelling.

To better visualise the dependence of the LFS density on fuelling and input power, the relative variation of the midplane density at different radial locations with fuelling rate is shown in figure 6 for two power levels (P_{in} = 9.2 MW and 14.6 MW) for discharge #30733. Densities at different locations were estimated for the time points indicated in figure 4 considering as a reference for the density variation the profiles at t = 2.35 s. As LFS profiles from reflectometry are not available up to the separatrix at high fuelling rates, Thomson scattering data is used for the confined region, lithium beam data for the separatrix and near SOL, and reflectometry in the far SOL. As shown before, the SOL and separatrix density increase with fuelling particularly at the highest fuelling rate while the SOL density doubles when the fuelling rate is varied by a factor of two. The density in the confined region does not change significantly. These results are in line with previous observations at JET (e.g. [30]). An increase in the input power

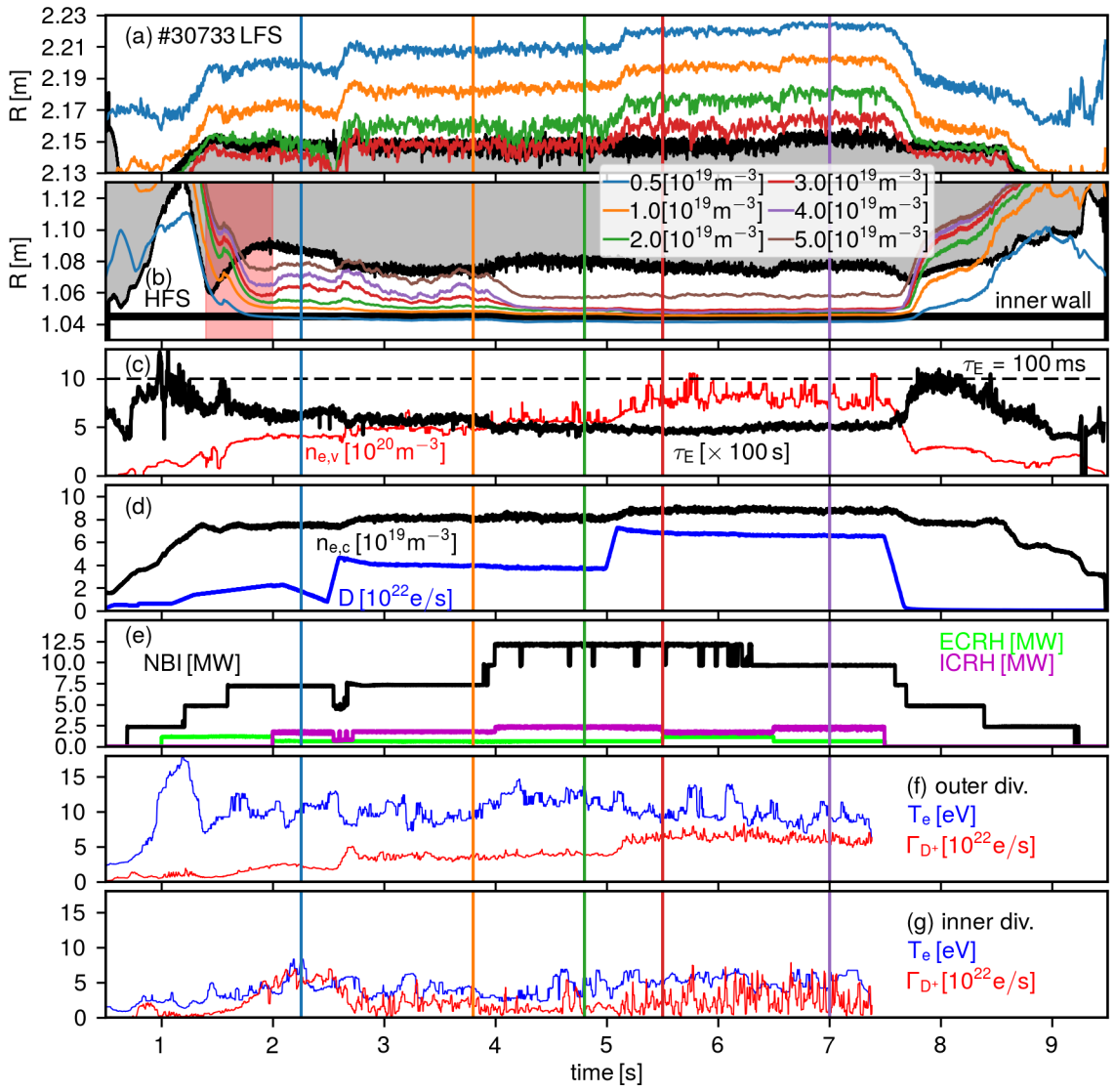

Figure 4: Trajectories of selected density layers at LFS (a) and HFS (b) for discharge #30773 from profile reflectometry; density in the divertor volume and τ_E (c); fuelling rate and central line-averaged density (d); NBI, ECRH, and ICRH heating power (e); Γ_{D^+} and T_e measured by Langmuir probes near the outer (f) and inner divertor strike-point (g). Reflectometry and Langmuir probe signals during ELMs have been removed.

(comparison between star and circle symbols at a fuelling rate of 4×10^{22} e/s) does not modify the LFS density in the confined region and leads to a modest density increase ($< 20\%$) in the SOL and at the separatrix.

Kallenbach et al. has shown recently [16] that the upstream LFS separatrix density for H-mode plasmas is strongly correlated with the outer divertor neutral pressure. Figure 7 displays the evolution of the neutral pressure in the inner and outer divertor again for discharge #30733 together with the estimated separatrix density at the LFS from reflectometry, $n_{sep,LFS}$ and lithium beam(LIN), $n_{sep,LIN}$. As HFS profiles from

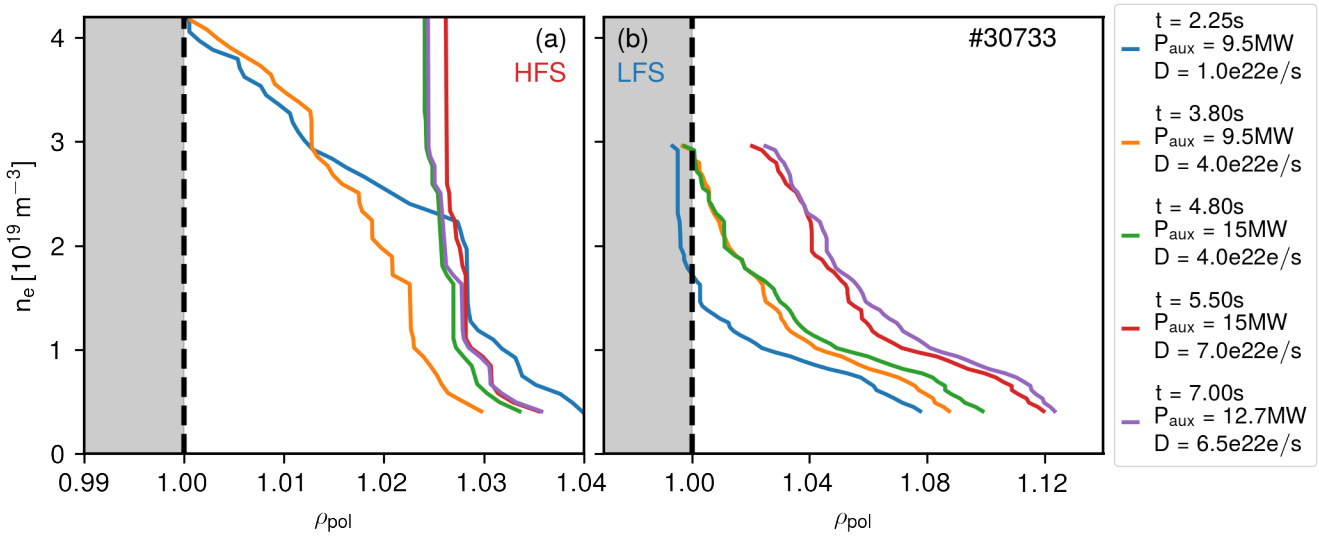

Figure 5: Evolution of the density profiles from reflectometry at (a) the HFS and (b) the LFS in normalised flux coordinates along the discharge #30733 for the time instants indicated in figure 4. Inter-ELM profiles are averaged over 200 ms and radially shifted at the HFS by 2.5 cm and at the LFS by −0.6 cm.

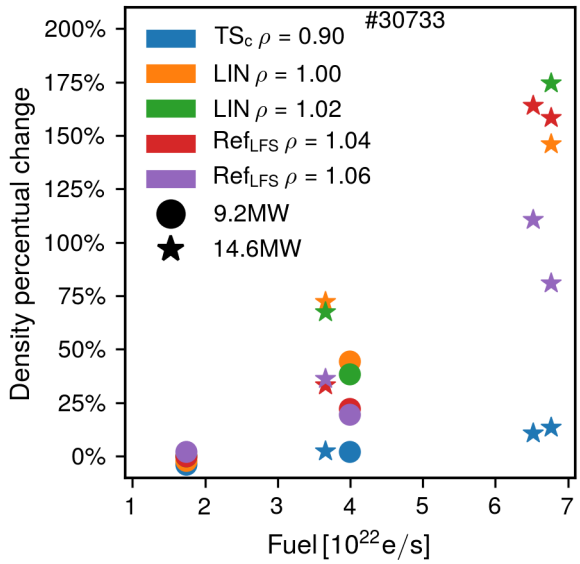

Figure 6: Relative variation of the LFS midplane density at different radial locations with fuelling for $P_{in} = 9.2\,MW$ (circles) and 14.6 MW (stars) for discharge #30733. Data for the confined region is from core Thomson scattering. Separatrix and $\rho = 1.02$ data is from the lithium beam diagnostic. Data from $\rho = 1.04$ and $\rho = 1.06$ is from reflectometry (inter-ELM data averaged over 200 ms).

reflectometry are often not available up to the separatrix due to the presence of the HFSHD, the density measured by reflectometry close to the inner vessel wall, $n_{wall,HFS}$,

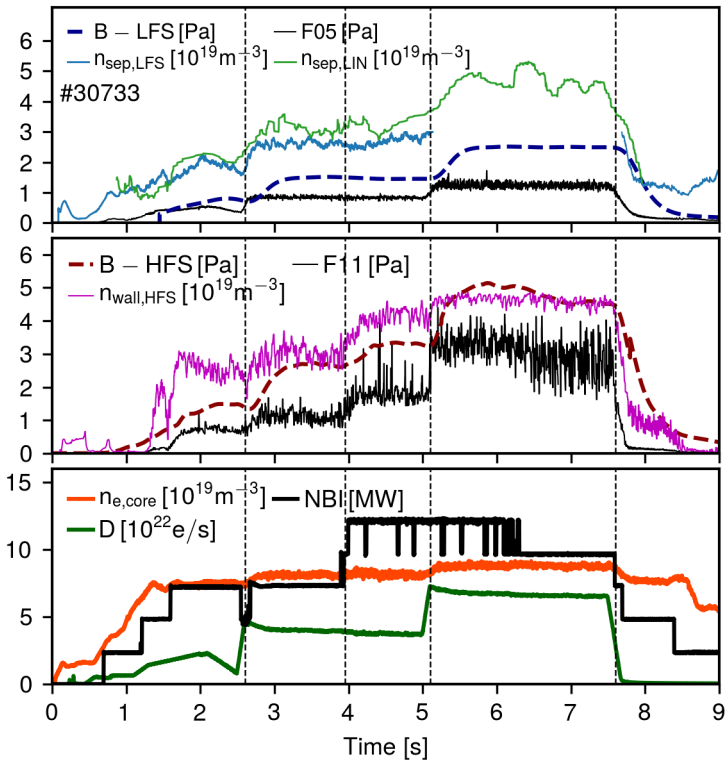

Figure 7: Top: Evolution of the neutral pressure measured by the baratrons (blue) and gauges (black) at outer divertor together with that of the LFS separatrix density estimated from reflectometry (cyan) and lithium beam (green). Middle: Evolution of the neutral pressure measured by the baratrons (dark red) and gauges (black) at inner divertor together with that of the density in front of the inner vessel wall (magenta) measured by reflectometry. Bottom: core line-averaged density (red), deuterium fuelling rate (green) and NBI heating power (black) for discharge #30733.

is shown. $n_{wall,HFS}$ is estimated as the maximum density in a vicinity of 5 mm from the inner wall to account for measurement inaccuracies. As shown in figure 7, the neutral pressure in both inner and outer target was found to respond strongly to the fuelling rate while responding to the input power only at the inner divertor. The evolution of the inner divertor neutral pressure is consistent with that of the HFSHD as both are observed to increase with fuelling and input power. An increase in the power to the SOL leads to an enhancement of the HFSHD and to an increase in the neutral pressure at the inner target but has a weak effect on the outer target and LFS midplane. The connection between the HFSHD and the LFS midplane profiles is therefore not always straightforward with respect to variations in the input power. Our results indicate that the separatrix density at the LFS is better correlated with the neutral pressure at the outer target while the HFS SOL density (the HFS separatrix density cannot be measured) follows the neutral pressure at the inner divertor.

5. Impact of the HFSHD front on the midplane density profile and confinement

The HFSHD front was suggested to lead to an outward shift of the density profile, which causes a degradation of stability, pedestal top pressure and global confinement [19]. A correlation is observed on AUG between the HFSHD formation and the evolution of the main plasma parameters such as confinement time or stored energy with respect to changes in impurity seeding [9, 19].

Our results confirm that seeding leads to a reduction of the HFSHD, to an inward shift of the density profile and to a confinement enhancement. This picture is further corroborated by the fact that an increase in the fuelling leads to an increase in the magnitude of the HFSHD associated with a degradation in confinement. The effect of the heating power also supports the suggested detrimental effect of the HFSHD on confinement. An increase in the heating power leads to a strong increase in the HFSHD and also to a degraded confinement, although with a slight confinement reduction.

The link between confinement and the HFSHD magnitude can be experimentally established by plotting the evolution along the discharge the average density in the divertor $n_{e,v}$ against the normalised confinement factor $H_{98,y2}$, the energy confinement time τ_E, and normalised beta β_N, see figure 8. Discharge #30554 was selected as it includes variations in the fuelling rate, input power and nitrogen seeding rate. A dashed line connects the data points chronologically to enable following the discharge evolution in time. At the beginning of the discharge, very low fuelling and additional heating are applied (blue dots) and a small magnitude HFSHD front is present, which is only seen by divertor spectroscopy when the D fuelling is ramped up. With the application of fuelling (dots in orange), confinement degrades and the HFSHD magnitude increases, reaching densities one order of magnitude higher than that at the LFS separatrix. In the later phase of the fuelling ramp, the confinement degradation is not associated with an increase of $n_{e,v}$. The reason for this observation is not clear but diagnostic limitations cannot be discarded. As described in section 2, the field of view of the divertor spectroscopy may not cover the full spatial extension of the HFSHD, which may lead to an underestimation of the divertor volume density. When the NBI power is stepped up and fuelling is further increased (green dots) the energy confinement time degrades marginally and the divertor density increases sharply. During this period τ_E and $H_{98,y2}$ have an opposite trend that is justified by the weaker confinement degradation with power with respect to the predicted by the $H_{98,y2}$ scaling [31]. Later, N seeding is applied (red triangles) leading to an improvement in confinement and to a mitigation of the HFSHD. Finally, with a further increase in NBI power, the divertor density increases again, with no significant changes in confinement (purple triangles). Data presented in figure 8 indicates that detrimental effect of the HFSHD on confinement is modest with respect to variations in the input power, contrary to the effect in the HFSHD. To further understand this observation the evolution along the discharge of β_N against $n_{e,v}$ is also analysed. As illustrated, the increase in the NBI heating power is

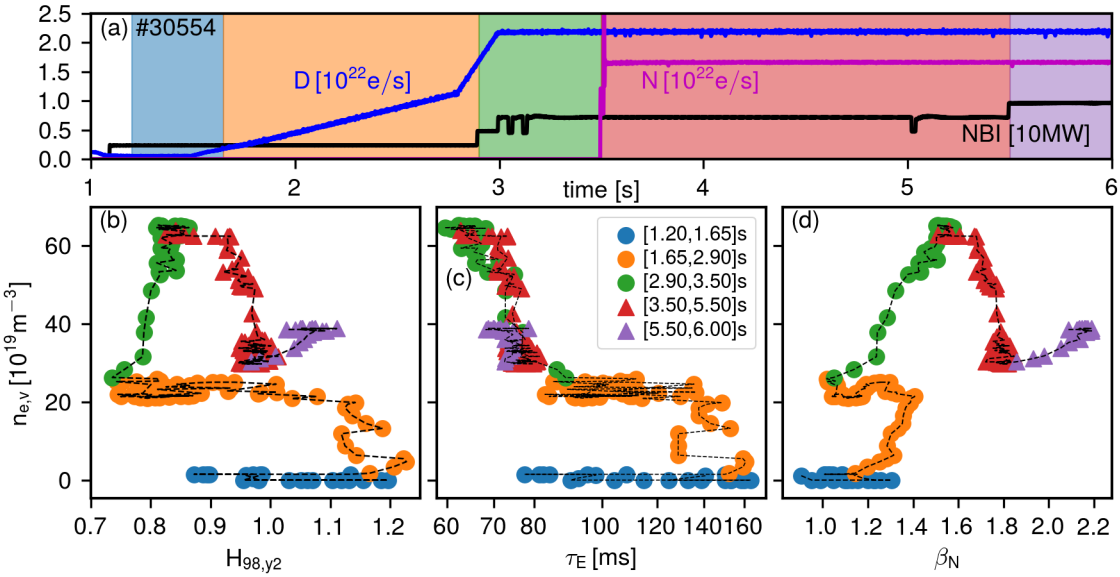

Figure 8: Top, (a): Evolution of NBI heating power, deuterium fuelling rate rate and N seeding for discharge #30554. Bottom: Divertor volume density $n_{e,v}$ as a function of: (b) confinement enhancement factor $H_{98,y2}$; (c) energy confinement time τ_E (in log scale); and (d) β_N. Color of the symbols correspond to shaded areas in (a). Triangle symbols correspond to the N seeded part of the discharge whilst circle symbols are from the unseeded part of the discharge.

associated with a significant rise in β_N. It is known that pedestal stability is influenced by the core pressure that increases with the heating power [32]. Therefore, our results suggest that the detrimental effect of the HFSHD may be partially overcompensated by the positive effect of increasing the heating power on energy confinement.

6. HFS/LFS asymmetries along the ELM cycle

A feature of H-modes are the edge localised modes (ELMs) [33] that cause quasi-periodic relaxations of the pedestal gradients in density and electron and ion temperature, expelling energy and particles into the SOL and consequently leading to transient heat and particle loads onto the divertor targets. Fast measurements of the SOL parameters are crucial to the understanding of ELM dynamics and for the evaluation of the fluxes to the plasma-facing components.

In this section, the evolution of the midplane density profiles along the ELM cycle is investigated. Experimental data from the HFS has rarely been reported in the literature (e.g. [34]) and therefore this work provides a unique opportunity to study the poloidal asymmetries during ELMs and to assess the importance of divertor condition in the midplane profiles. Since O-mode reflectometry cannot measure inverted gradients in density profiles, no conclusions can be made about the role of filamentary activity during the ELM that may lead to hollow density profiles (particularly at the LFS SOL)

associated with the expulsion of the filamentary structures (e.g. [35]).

In order to establish the effect of the different plasma parameters and divertor conditions on the midplane profiles, discharge #30554 was again selected now with a focus in the ELM evolution. In the first H-mode phase, moderate NBI power and gas fuelling are applied resulting in large amplitude low frequency (50 Hz) ELMs. Figure 9 displays the evolution of the iso-density layers at the HFS and LFS for type-I ELMs during the first phase of discharge #30554 together with the particle flux, electron temperature, divertor shunt current (divertor currents measured via shunt resistors connected to the divertor target modules [36]) and D_α emission at the inner and outer divertor targets. During this phase the fuelling rate and input power are moderate and inter-ELM midplane density profiles are roughly symmetric as shown previously. Nevertheless, as illustrated in figure 9, clear HFS/LFS asymmetries are observed after the ELM crash for about 5 ms. Density layers at the LFS present the classical evolution corresponding to the ELM crash with SOL layers moving outwards. The observed time scales correspond to the typical ELM evolution on AUG with a collapse time in the order of 1 ms and a recovery in the order of 2 ms.

The evolution of the HFS density layers is dramatically different. The ELM leads to a large increase in the SOL density characterised first by a fast evolution in a time scale below 1 ms that is then followed by a slower outward movement of the layers with higher density up to $t - t_{ELM} \approx 2 - 3$ ms (t_{ELM} is defined as the beginning of the ELM crash). Afterwards, the profiles recover slowly reaching the pre-ELM profile only around 10 ms after the ELM crash. An HFS/LFS asymmetry in the midplane density is observed already during the pedestal collapse period, with the asymmetry getting stronger during the ELM recovery. This conclusion was already hinted from the evolution of the asymmetry parameter shown in figure 3g, revealing that this parameter exhibits strong variation during the large type-I ELMs. The behaviour of the HFS midplane profile appears to be correlated with the detachment evolution at the divertor. The evolution in the divertor conditions is strongly influenced by the pedestal parameters during ELMs because transient changes in the heat and particle fluxes across the separatrix cause a strong modification in the SOL and divertor plasma.

A more detailed description of the evolution of the inner and outer divertor conditions along the ELM cycle can be obtained from the divertor Langmuir probes signals, displayed in figure 9d,e. The large pre-ELM D_α emission at the inner target as well as the low Γ_{D^+} and T_e (that is below 5 eV) suggest that the inner divertor is at least partially detached before the ELM occurs. During the ELM crash the D_α radiation is reduced and the target Γ_{D^+} and T_e increase that can be interpreted as the inner divertor target becoming attached due to the particle and energy losses from the pedestal to the divertor. At about $t - t_{ELM} \approx 2$ ms the D_α radiation rises and the Γ_{D^+} and T_e are reduced again indicating a detachment of the inner target after the ELM. The degree of detachment is then reduced again around $t - t_{ELM} \approx 5$ ms as indicated by the increase in Γ_{D^+} and T_e.

The outer divertor plasma is attached before the ELM with Γ_{D^+} and T_e increasing

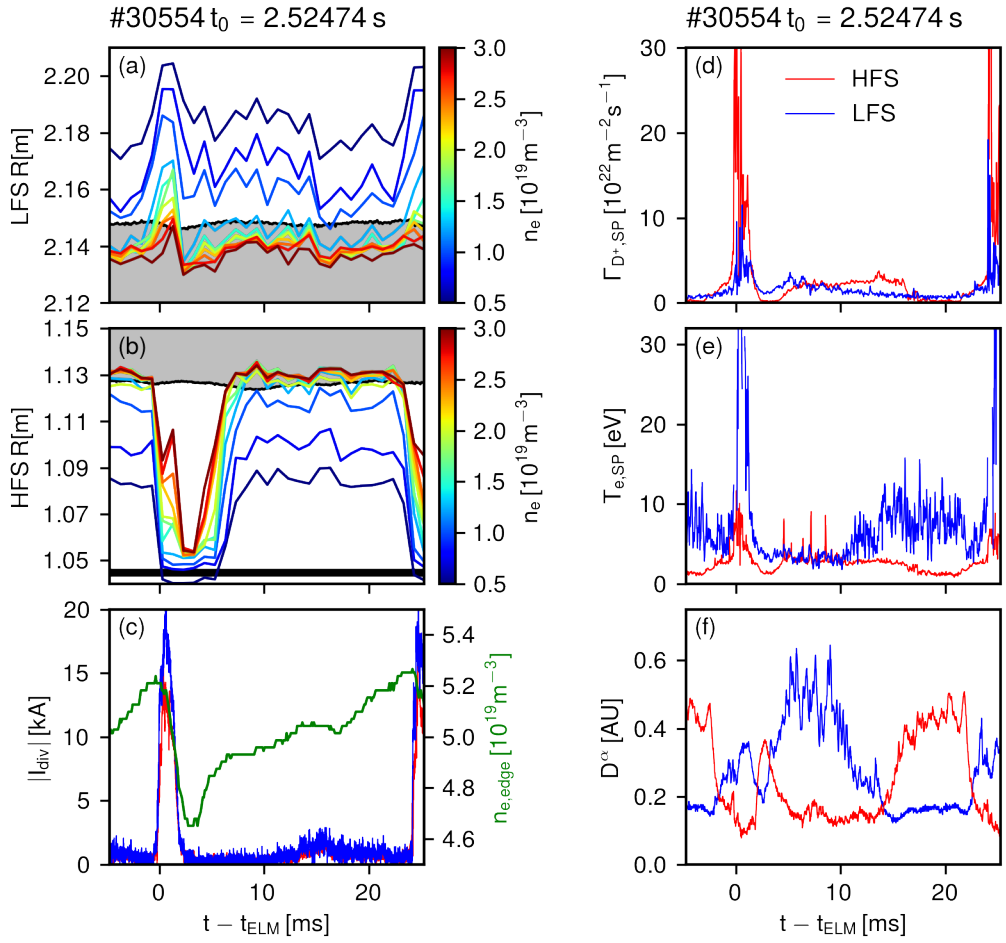

Figure 9: Evolution of the density layers from reflectometry at the LFS (a) and HFS (b) during a type-I ELM; divertor shunt current for the LFS (blue) and HFS (red), together with the density from the edge interferometer (in green) (c); particle flux at the LP closest to the inner (red) and outer (blue) strike-point(d); electron temperature from the same LP (e); and D_α radiation at the inner (red) and outer (blue) divertor(f).

during the ELM crash. Then, starting around $t - t_{ELM} \approx 2\,ms$ and for a period of about $7 - 8\,ms$, the electron temperature is reduced to $\approx 5\,eV$ and D_α emission increases indicating that the outer divertor is partially detached. After $\approx 10\,ms$, the outer target re-attaches again (increase in T_e and decrease in D_α) until the next ELM occurs. We can conclude that just after the ELM crash, as the LFS density profiles recover, the outer divertor is in partial detachment and the inner divertor target is fully detached. Interestingly, in the period from 4 ms to 8 ms the divertor parameters near the strike-point are roughly similar at the inner and outer divertor region suggesting a similar state of detachment. Afterwards, the detachment conditions have an opposite evolution at the inner and outer target, becoming more detached at the inner and more attached at the outer divertor. The increase in the outer divertor temperature around 12 ms may cause additional particle fluxes from the outer divertor into the private-flux region

and from the private-flux region into the inner divertor [15], leading to a high density and low temperature in the inner divertor and promoting the detachment of the inner divertor.

The period with a high degree of detachment at the inner divertor ($2 < t - t_{ELM} < 5$ ms) corresponds to the phase were the measured density at the inner vessel wall is very high, suggesting the existence of a HFSHD front during this period. Although the temporal resolution of the Stark broadening diagnostic does not permit following the evolution of the divertor HFSHD during the ELM cycle, the fact that the inner target is fully detached strongly suggests that a HFSHD is present at the inner divertor just after the ELM event. After 5 ms, the inner divertor moves to a partially detached state and a corresponding decrease of the midplane HFSHD is seen with the density profiles returning to pre-ELM values.

To overcome the limitation resulting from the modest temporal resolution of the reflectometry diagnostic, data from the different phases of discharge #30554 have been conditionally averaged to obtain the typical evolution of the ELM for each phase using as reference the time of the ELM crash. Figure 10 displays the evolution of the iso-density layers at the HFS and LFS for average type-I ELMs during the first phase of discharge #30554 together with the particle flux to the inner and outer divertor target, also conditionally averaged. As expected, the main features described above for the evolution along the ELM cycle are also seen in the conditionally averaged signals.

The LFS density profiles at the midplane exhibit a fast recovery of the midplane density profiles ($2 - 3$ ms). About $3 - 4$ ms after the ELM crash an increase in the SOL density is observed that coincides with the changes in the divertor conditions. An increase in the degree of detachment in the outer divertor is seen in a period where the inner target in strongly detached and a HFSHD is present. The increased divertor heat load due to ELMs leads to a temporary re-attachment of the outer divertor during ≈ 2 ms after the ELM crash with the divertor plasma becoming detached again after this period as indicated by the particle flux measured by the divertor probes. When studying the effect of fuelling and heating power on the inter-ELM profiles, SOL profiles at the midplane have been observed to broaden as detachment is enhanced. The broadening of the LFS SOL density profiles at the midplane after a fast recovery of the profiles may therefore be associated with changes in the divertor conditions.

Recent studies on the ELM evolution in AUG utilising several divertor, SOL and pedestal diagnostics [37] have found that the magnetic activity during the density pedestal recovery is low and consequently the particle flux across the edge is modest. Approximately 3 ms after the ELM onset, medium frequency fluctuations between 30 kHz and 150 kHz set in that are temporally correlated to the stagnation of the density pedestal recovery and the increase in the SOL density that coincides with the changes in the divertor conditions.

Conditionally averaged profiles also confirm that the evolution of the density layers at LFS and HFS is significantly different with a HFSHD forming after the ELM crash. As illustrated in figure 10, the conditionally averaged particle flux to the divertor is strongly

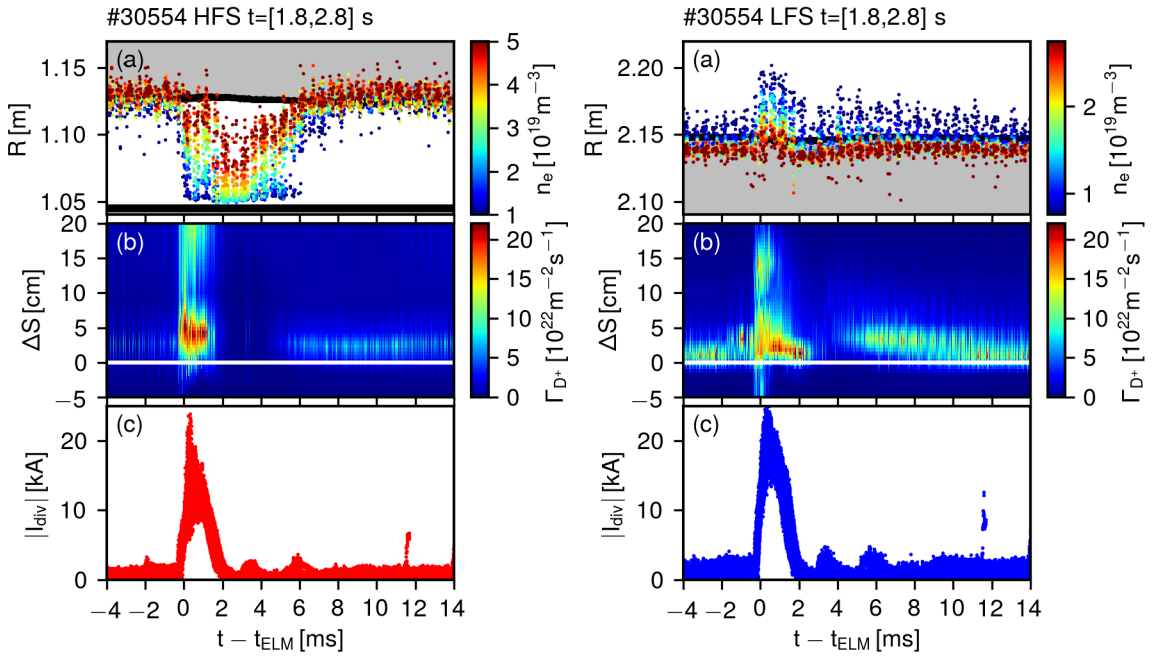

Figure 10: Phase I of #30554; (a): Evolution of the conditional averaged density layers from reflectometry at the HFS (left) and LFS (right) for ELMs in the time interval $t = [1.8, 2.8]$ s; (b): conditional averaged particle flux to the inner and outer divertor target; (c): divertor shunt current. The ΔS coordinate is the distance from the strike-point along the divertor target.

reduced across the entire region explored by the target probes suggesting that the inner target is completely detached. This leads to the formation of a HFSHD extending up to the midplane and resulting in the large SOL densities observed at the HFS by the reflectometry diagnostic. The inner divertor is observed to detach before the outer one and to reach a higher degree of detachment (stronger reduction in Γ_{D^+} and T_e). The HFSHD is caused by the increased particle and heat fluxes to the inner divertor induced by the ELM and is extinguished after the ELM when the energy required to sustain the HFSHD is no longer available and the degree of detachment of the inner divertor is reduced. Our results suggest again that the evolution of the HFS density profiles along the ELM cycle is strongly influenced by the divertor conditions.

In the second phase of the discharge #30554, both NBI power and gas fuelling are increased, leading to more frequent ELMs. This phase is characterised by the presence of a HFSHD and large HFS/LFS asymmetries in the inter-ELM period as described previously. As displayed in figure 11, the ELM evolution during this phase is basically very similar to that observed in the first phase but now HFS profiles do not fully recover. The HFSHD exists during the entire inter-ELM period. Density profiles do not become HFS/LFS symmetric at the end of the ELM cycle as observed in the first phase.

The minimum in the LFS SOL density width at $t - t_{ELM} \approx 2 - 3$ s again seems to be correlated with the evolution of the outer target detachment. The temporal evolution

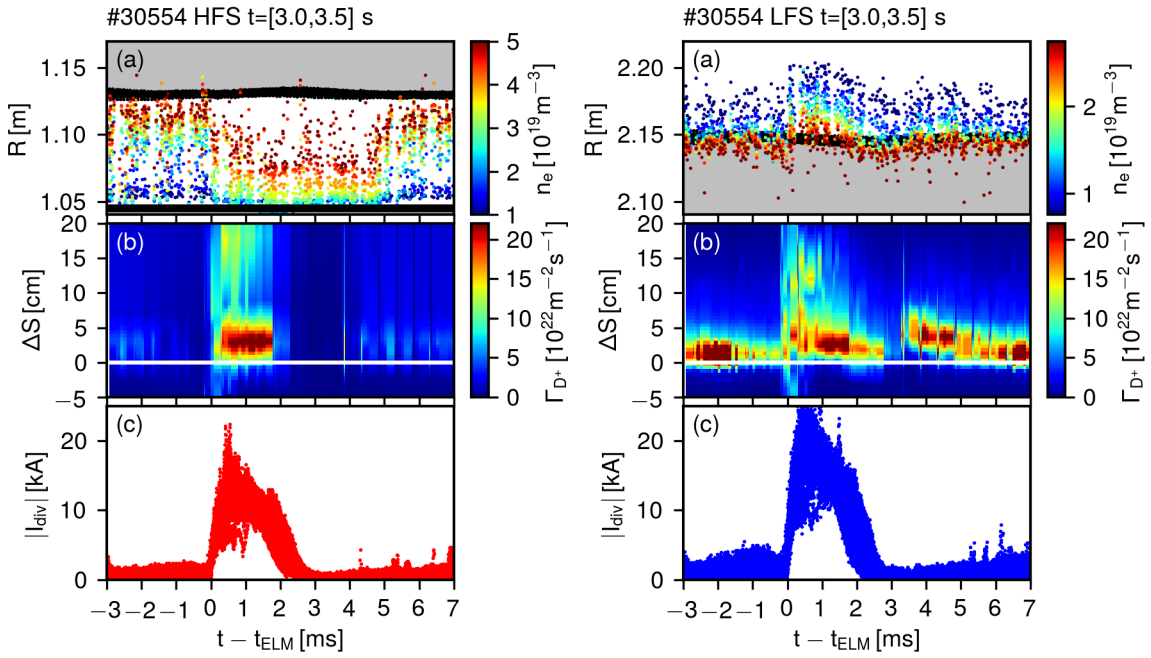

Figure 11: Phase II of #30554; (a): Evolution of the conditional averaged density layers from reflectometry at the HFS (left) and LFS (right) for ELMs in the time interval $t = [3.0, 3.5]$ s; (b) conditional averaged particle flux to the inner and outer divertor target; (c): divertor shunt current.

of the divertor quantities is also very similar to that in the previous phase with the main difference being that the partially detached phase is now shorter, possibly a consequence of the higher ELM frequency.

Seeding strongly influences the divertor conditions and therefore it is also expected to modify the evolution of the midplane density during ELMs. The ELM frequency increases to 190 Hz meaning that the duration of the ELM cycle used in the conditional average technique has now to be reduced. However, the evolution of the LFS profiles is generally similar. The drop in the pedestal density is now modest and, consequently, the particle flux to the divertor is reduced with respect to that observed in the previous phases.

On the contrary, the density evolution at the HFS midplane changes dramatically when seeding is injected. As a result of the reduction in the divertor HFSHD, the HFS/LFS density asymmetry is now smaller with the ELM density perturbation occurring only during a short period below 1 ms with a secondary peak observed about ≈ 2 ms after. The particle flux to the inner target during the ELM crash is now significantly smaller, possibly explaining that no HFSHD is formed after the ELMs during the seeded phase. The inner divertor is completely detached (as indicated by the modest particle flux) but no HFSHD exists at the midplane. This is justified by the seeding promoting detachment while reducing the HFSHD, as the power reaching the inner divertor is reduced by radiation in the SOL and the E × B drift across the private

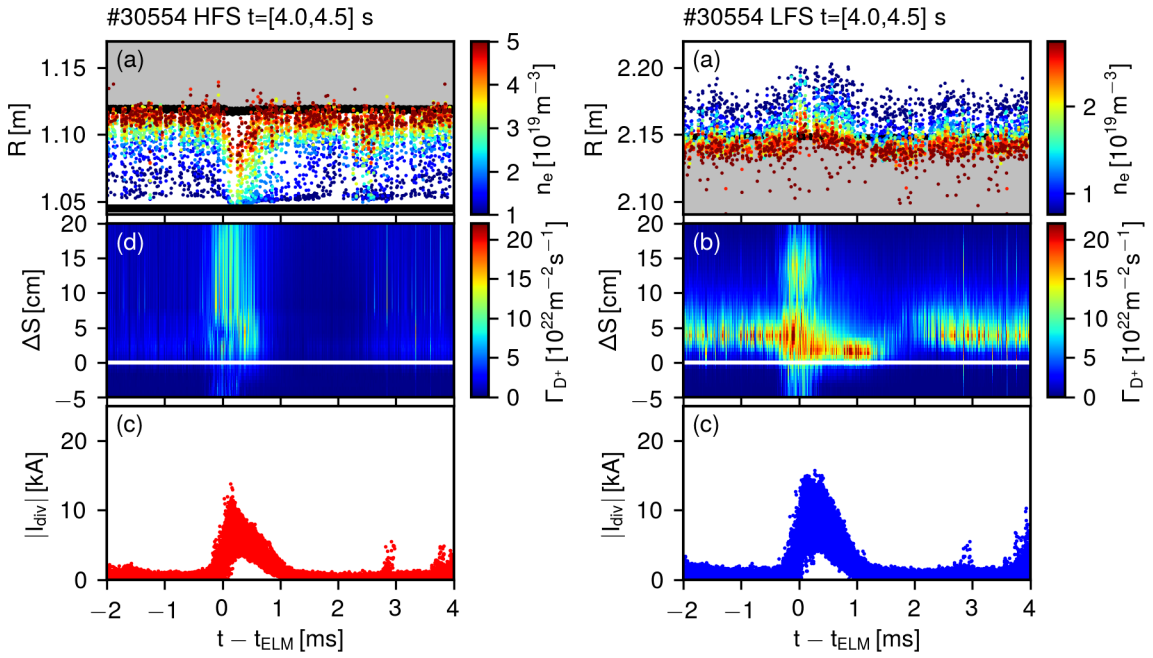

Figure 12: Phase III of #30554; (a): Evolution of the conditional averaged density layers from reflectometry at the HFS (left) and LFS (right) for ELMs in the time interval $t = [4.0, 4.5]$ s; (b): conditional averaged particle flux to the inner and outer divertor target; (c): divertor shunt current.

flux region is reduced because of the cooler outer divertor.

In summary, it has been possible to achieve a comprehensive characterisation of the ELM evolution at the midplane and divertor. The strong effect of the divertor conditions on the SOL density at the midplane is again demonstrated. The most striking result is the observation of a HFSHD at the midplane just after the ELM crash associated with the strong inner divertor detachment. ELMs modify the detachment conditions due to the increased power and particle input to the SOL and in the radiation losses that then reacts back to the midplane SOL parameters and possibly affecting also the pedestal and confinement properties.

The LFS density profiles at the midplane were found to exhibit a faster recovery than at the HFS. However, about $3 - 4$ ms after the ELM crash an increase in the LFS SOL density is observed that can relate to changes in the divertor conditions or to changes in transport in the pedestal [37]. A key element of the study presented here is the ability to measure density profiles at the LFS and HFS during ELMs and relate it to the evolution of the divertor detachment by combining data from several diagnostics.

7. Discussion and summary

Results presented in this paper demonstrate that asymmetries between LFS and HFS density profiles at the midplane exist in H-mode. In ASDEX Upgrade with a tungsten

wall, LFS/HFS symmetric density profiles are rarely observed, occurring only in low heating power H-modes discharges. Similarly to L-mode discharges, the HFSHD front and its effect on the midplane density profiles evolve with detachment of the inner divertor not existing when this divertor region is fully attached. Particularly relevant for this work is the contribution of the O-mode reflectometry diagnostic installed at the AUG midplane to a better characterisation of the underdiagnosed HFS region.

Fuelling and heating power have different effects on the density profile. Fuelling causes an increase in the separatrix density at the LFS in line with previous observations (e.g. [16]), since higher fuelling corresponds to higher neutral pressure in the outer divertor. There is an overall increase in the SOL density with fuelling, particularly near the separatrix while in the confined region the effect is not as pronounced. On the HFS, fuelling also increases the SOL density as a result of the enhancement of the HFSHD.

Heating power has a different effect. While only producing a modest effect on the LFS density profile, changes in heating power greatly affect the HFS density profiles where the HFSHD forms promptly in the divertor at modest power values. When the NBI heating power is increased, the HFS density profiles move rapidly to the inner vessel wall, signaling that the HFSHD becomes large enough to manifest itself at the midplane. Our results indicate that the separatrix density at the LFS is better correlated with the neutral pressure at the outer target while the HFS SOL density follows the neutral pressure at the inner divertor.

Nitrogen seeding leads to a reduction of the HFSHD front and to a reduction of the SOL density (at both the LFS and HFS). Simultaneously, confinement is enhanced in agreement with previous observations [19]. A correlation between the reduction of the HFSHD and confinement improvement is confirmed corroborating previous observations [9, 19], particularly with respect to variations in seeding and fuelling rate. However, the detrimental effect of the HFSHD on confinement is often modest with respect to variations in the input power, contrary to the effect in the HFSHD.

A comprehensive characterisation of the ELM evolution at the midplane and divertor is performed demonstrating that also during the ELM cycle the evolution of the divertor conditions are correlated with the SOL density at the midplane. The most striking result is the observation of a HFSHD at the midplane just after the ELM crash associated with strong inner divertor detachment. ELMs modify the detachment conditions due to the increased power and particle input to the SOL that then reacts back to the midplane SOL parameters, particularly at the HFS, possibly affecting also the pedestal and confinement properties.

Our experimental studies contribute to the growing evidence that divertor and midplane parameters are strongly linked both at the LFS and the HFS.

8. Acknowledgements

This work has been carried out within the framework of the EUROfusion Consortium and has received funding from the Euratom research and training programme 2014-

2018 and 2019-2020 under grant agreement No 633053. IST activities also received financial support from "Fundação para a Ciência e Tecnologia" through project UID/FIS/50010/2019 and grant SFRH/BD/87738/2012. The views and opinions expressed herein do not necessarily reflect those of the European Commission.

The author would also like to acknowledge the efforts of the open-source community that developed the tools employed for the analysis performed in this work, namely matplotlib [38].

References

[1] Wagner F, Becker G, Behringer K, Campbell D, Eberhagen A, Engelhardt W, Fussmann G, Gehre O, Gernhardt J, Gierke G v *et al.* 1982 *Physical Review Letters* **49** 1408

[2] LaBombard B and Lipschultz B 1987 *Nuclear Fusion* **27** 81–99 ISSN 0029-5515

[3] Krasheninnikov S 1998 *Czechoslovak journal of physics* **48** 97–112

[4] Bernert M, Eich T, Kallenbach A, Carralero D, Huber A, Lang P T, Potzel S, Reimold F, Schweinzer J, Viezzer E and Zohm H 2014 *Plasma Physics and Controlled Fusion* **57** 014038

[5] Wang L, Guo H, Ding F, Yu Y, Yuan Q, Xu G and Wang H 2019 *Nuclear Fusion*

[6] Petrie T, Allen S, Carlstrom T, Hill D, Maingi R, Nilson D, Brown M, Buchenauer D, Evans T, Fenstermacher M *et al.* 1997 *Journal of nuclear materials* **241** 639–644

[7] Kallenbach A, Bernert M, Beurskens M, Casali L, Dunne M, Eich T, Giannone L, Herrmann A, Maraschek M, Potzel S, Reimold F, Rohde V, Schweinzer J, Viezzer E, Wischmeier M and the ASDEX Upgrade Team 2015 *Nuclear Fusion* **55** 053026

[8] McCormick K, Dux R, Fischer R, Scarabosio A *et al.* 2009 *Journal of Nuclear Materials* **390** 465–469

[9] Potzel S, Dunne M, Dux R, Guimarais L, Reimold F, Scarabosio A and Wischmeier M 2015 On the high density in the HFS far SOL at ASDEX Upgrade and its impact on plasma confinement *42nd European Physical Society Conference on Plasma Physics, EPS 2015*

[10] Potzel S, Wischmeier M, Bernert M, Dux R, Reimold F, Scarabosio A, Brezinsek S, Clever M, Huber A, Meigs A *et al.* 2015 *Journal of Nuclear Materials* **463** 541–545

[11] Potzel S, Wischmeier M, Bernert M, Dux R, Reimold F, Scarabosio A, Brezinsek S, Clever M, Huber A, Meigs A and Stamp M 2015 *Journal of Nuclear Materials* **463** 541–545 ISSN 00223115

[12] Potzel S, Wischmeier M, Bernert M, Dux R, Müller H and Scarabosio A 2014 *Nuclear Fusion* **54** 013001 ISSN 0029-5515

[13] Potzel S, Wischmeier M, Bernert M, Dux R, Müller H W and Scarabosio A 2013 *Journal of Nuclear Materials* **438** ISSN 00223115

[14] Reimold F, Wischmeier M, Bernert M, Potzel S, Kallenbach A, Müller H W, Sieglin B, Stroth U and the ASDEX Upgrade Team 2015 *Nuclear Fusion* **55** 033004 ISSN 0029-5515

[15] Reimold F, Wischmeier M, Potzel S, Guimarais L, Reiter D, Bernert M, Dunne M, Lunt T *et al.* 2017 *Nuclear Materials and Energy* **12** 193–199

[16] Kallenbach A, Sun H, Eich T, Carralero D, Hobirk J, Scarabosio A, Siccinio M, EUROfusion M *et al.* 2018 *Plasma Physics and Controlled Fusion* **60** 045006

[17] Loarte A, Monk R, Martín-Solís J, Campbell D, Chankin A, Clement S, Davies S, Ehrenberg J, Erents S, Guo H, Harbour P, Horton L, Ingesson L, Jäckel H, Lingertat J, Lowry C, Maggi C, Matthews G, McCormick K, O'Brien D, Reichle R, Saibene G, Smith R, Stamp M, Stork D and Vlases G 1998 *Nuclear Fusion* **38** 331–371 ISSN 0029-5515

[18] Frassinetti L, Dodt D, Beurskens M, Sirinelli A, Boom J, Eich T, Flanagan J, Giroud C, Jachmich M, Kempenaars M *et al.* 2015 *Nuclear Fusion* **55** 023007

[19] Dunne M G, Potzel S, Reimold F, Wischmeier M, Wolfrum E, Frassinetti L, Beurskens M, Bilkova P, Cavedon M, Fischer R, Kurzan B, Laggner F M, McDermott R M, Tardini G, Trier E, Viezzer E, Willensdorfer M, Team T E M and Team T A U 2017 *Plasma Physics and Controlled Fusion* **59** 014017

[20] Guimarais L, Potzel S, Silva C, Bernert M, Carralero D, Conway G, Gil L, Manso M, Nikolaeva V, Reimold F, Santos J, Silva A, Stroth U, Vicente J, Wischmeier M and Wolfrum E 2018 *Nuclear Fusion* **58** 026005 ISSN 0029-5515

[21] Silva A, Manso M E, Cupido L, Albrecht M, Serra F, Varela P, Santos J, Vergamota S, Eusebio F, Fernandes J, Grossmann T, Kallenbach A, Kurzan B, Loureiro C, Meneses L, Nunes I, Silva F and Team W S A U 1996 *Review of Scientific Instruments* **67** 4138–4145 ISSN 00346748

[22] Varela P, Manso M, Nunes I, Santos J, Nunes F, Silva A and Silva F 1999 *Review of scientific instruments* **70** 1060–1063

[23] Santos J, Guimarais L, Zilker M, Treutterer W and Manso M 2012 *Nuclear Fusion* **52** ISSN 00295515 17414326

[24] Schneider P, Orte L B, Burckhart A, Dunne M, Fuchs C, Gude A, Kurzan B, Suttrop W, Wolfrum E *et al.* 2014 *Plasma Physics and Controlled Fusion* **57** 014029

[25] Weinlich M and Carlson A 1996 *Contributions to Plasma Physics* **36** 53–59

[26] Scarabosio A, Haas G, Müller H, Pugno R, Wischmeier M *et al.* 2009 *Journal of Nuclear Materials* **390** 494–497

[27] Reimold F, Wischmeier M, Bernert M, Potzel S, Coster D, Bonnin X, Reiter D, Meisl G, Kallenbach A, Aho-Mantila L *et al.* 2015 *Journal of Nuclear Materials* **463** 128–134

[28] Reimold F, Kukushkin A, Wischmeier M, Bernert M and Reiter D *Preprint: 2016 IAEA Fusion Energy Conference, Kyoto [EX/P6-22]*

[29] Kalman R E 1960 *Journal of basic Engineering* **82** 35–45

[30] Maggi C, Saarelma S, Casson F, Challis C, de la Luna E, Frassinetti L, Giroud C, Joffrin E, Simpson J, Beurskens M *et al.* 2015 *Nuclear Fusion* **55** 113031

[31] Verdoolaege G, Kaye S M, Angioni C, Kardaun O, Maslov M, Romanelli M, Ryter F and Thomsen K *Preprint: 2018 IAEA Fusion Energy Conference, Gandhinagar [EX/P7-1]*

[32] Wolfrum E, Beurskens M, Dunne M, Frassinetti L, Gao X, Giroud C, Hughes J, Lunt T, Maingi R, Osborne T *et al.* 2017 *Nuclear Materials and Energy* **12** 18–27

[33] Zohm H 1996 *Plasma Physics and Controlled Fusion* **38** 105

[34] Kirk A, Wilson H, Akers R, Conway N, Counsell G, Cowley S, Dowling J, Dudson B, Field A, Lott F *et al.* 2005 *Plasma physics and controlled fusion* **47** 315

[35] Scannell R, Kirk A, Ayed N B, Carolan P, Cunningham G, McCone J, Prunty S and Walsh M 2007 *Plasma Physics and Controlled Fusion* **49** 1431

[36] Kallenbach A, Dux R, Fuchs J, Fischer R, Geiger B, Giannone L, Herrmann A, Lunt T, Mertens V, McDermott R *et al.* 2010 *Plasma Physics and Controlled Fusion* **52** 055002

[37] Laggner F M, Keerl S, Gnilsen J, Wolfrum E, Bernert M, Carralero D, Guimarais L, Nikolaeva V, Potzel S, Cavedon M, Mink F, Dunne M G, Birkenmeier G, Fischer R, Viezzer E, Willensdorfer M, Wischmeier M, Aumayr F, the EUROfusion MST1 Team and the ASDEX Upgrade Team 2018 *Plasma Physics and Controlled Fusion* **60** 025002

[38] Hunter J D 2007 *Computing In Science & Engineering* **9** 90–95